JOURNAL OF THEORETICAL AND APPLIED MECHANICS
55, 4, pp. 1219-1233, Warsaw 2017
DOI: 10.15632/jtam-pl.55.4.1219

EXPERIMENTAL AND NUMERICAL ANALYSIS OF ALUMINUM ALLOY AW5005 BEHAVIOR SUBJECTED TO TENSION AND PERFORATION UNDER DYNAMIC LOADING

Amine Bendarma
Poznan University of Technology, Institute of Structural Engineering, Poznań, Poland, and Universiapolis, Ecole Polytechnique d'Agadir Bab Al Madina, Qr Tilila, Agadir, Morocco
e-mail: b.amine@e-polytechnique.ma

Tomasz Jankowiak, Tomasz Łodygowski
Poznan University of Technology, Institute of Structural Engineering, Poznań, Poland
e-mail: tomasz.jankowiak@put.poznan.pl; tomasz.lodygowski@put.poznan.pl

Alexis Rusinek
Laboratory of Mechanics, Biomechanics, Polymers and Structures (LaBPS), National Engineering School of Metz (ENIM), Metz, France; e-mail: alexis.rusinek@univ-lorraine.fr

Maciej Klósak
Universiapolis, Ecole Polytechnique d'Agadir Bab Al Madina, Qr Tilila, Agadir, Morocco, and The International University of Logistics and Transport in Wrocław, Poland
e-mail: klosak@e-polytechnique.ma

The paper describes mechanical behavior of aluminum alloy AW5005 (EN AW5005) under impact loading. The work is focused on tensile tests and the process of perforation of aluminum alloy AW5005 sheets. Experimental, analytical and numerical investigations are carried out to analyse in details the perforation process. Based on these approaches, ballistic properties of the structure impacted by a conical nose shape projectile are studied. Different failure criteria are discussed, coupling numerical and experimental analyses for a wide range of strain rates. Optimization method functions are used to identify the parameters of the failure criteria. Finally, good correlation is obtained between the numerical and experimental results for both tension and perforation tests.

Keywords: aluminum alloy, AW5005, ballistic behavior, failure criterion

1. Introduction

In this paper, a study on aluminum alloy AW5005 behavior is reported. This alloy contains nominally 0.8% magnesium and it presents a medium strength, good weldability and good corrosion resistance in marine atmospheres. The metallurgical state of the aluminum alloy used in this work is as received. It has a lower density and an excellent thermal conductivity compared to other aluminum alloys. It is the most commonly used type of aluminum in sheet and plate forms (Kulekci, 2014).

The ballistic behavior and resistance of aluminum sheet plates is strongly dependent on the material behavior under dynamic loading. The ballistic properties of the structure are intensely related to the material behavior and to the interaction between the projectile and a thin aluminum target during the perforation process. Therefore, to find expected curves, many dynamic constitutive relations have been studied in several works. For instance, Johnson and Cook (1983) proposed a dynamic constitutive relation based on a phenomenological approach. The model has

been often used in impact and perforation problems analysis. Verleysen *et al.* (2011) investigated the effect of strain rate on the forming behavior of sheet metals and described stress-strain curves of the material using the Johnson-cook model. Erice *et al.* (2014) presented a coupled elastoplastic-damage constitutive model to simulate the failure behavior of inconel plates. Rusinek and Rodríguez-Martínez (2009) provided two extensions of the original Rusinek-Klepaczko constitutive relation (Rusinek and Klepaczko, 2001) in order to define the behavior of aluminum alloys at wide ranges of strain rates and temperatures showing a negative strain rate sensitivity. Børvik *et al.* (2009) studied the influence of a modified Johnson-Cook constitutive relation using numerical simulations of steel plate perforation. Jankowiak *et al.* (2013) considered perforation of different configurations: mild steel and sandwich plates. The effectiveness of these kinds of structures was checked. The authors also presented the effect of strain rate sensitivity models (Johnson-Cook and Rusinek-Klepaczko) on the ballistic curve. Additionally, several effects were considered: strain hardening, yield stress and projectile mass. Based on these results, it was possible to optimize the structure and find the right plate thickness to prevent its perforation. The sandwich configuration containing two sheets of steel is less efficient than a monolithic steel sheet of an equivalent total thickness. It was proven that thickness of the target had an important effect on the ballistic performance. This analysis can be used for the present AW5005 structure optimization. Kpenyigba *et al.* (2013) and Rusinek *et al.* (2008) studied the influence of the projectile nose shape (conical, blunt and hemispherical) and the projectile diameter on ballistic properties and failure modes of thin steel targets. In order to simulate the behavior of impacted and perforated structures, the finite element method with an explicit time integration procedure was an effective technique (Kpenyigba *et al.*, 2013; Rusinek *et al.*, 2008; Rusinek and Rodríguez-Martínez, 2008; Quinney and Taylor, 1937; Xue and Belytschko, 2010). Numerical simulations, in particular by the FE method, are also effective supplements for theoretical and experimental investigations which were carried out to analyze the dynamic behavior of impacted structures.

In order to determine mechanical characteristics of the material in quasi-static conditions, tensile tests have been carried out according to the methodology discussed in (Zhong *et al.*, 2016).

2. Experimental approach

There are little references about this material, especially concerning mechanical properties of this specific aluminum alloy. However, Kulekci (2014) published that the yield strength is equal to 45 MPa and the tensile strength is 110 MPa. Additionally, it is described that the elongation of this alloy is close to 15%. In the present paper, a tensile test is used to calibrate the material behavior. The specimen is machined from a 1.0 mm thickness aluminum sheet. The dimensions of the specimen are presented in Fig. 1. Additionally, the perforation test is used to describe ballistic properties of the material and failure modes for the conical projectile nose shape see Fig. 4. Compression using a sandwich specimen (Zhong *et al.*, 2015) and shear tests (Rusinek and Klepaczko, 2001; Bao and Wierzbicki, 2004) also reports for this material but it is out of scope of this analysis.

2.1. Tensile test

Quasi-static uniaxial tensile tests of AW5005 aluminum have been performed using a conventional hydraulic machine. The dimensions of the flat dumbbell-shaped specimen are shown in Fig. 1 (Zhong *et al.*, 2016). The first part of the specimen is embedded on 40 mm while the other end of the specimen is fixed to the mobile crosshead. The loading force and the displacement are recorded during the tests for the imposed velocity.

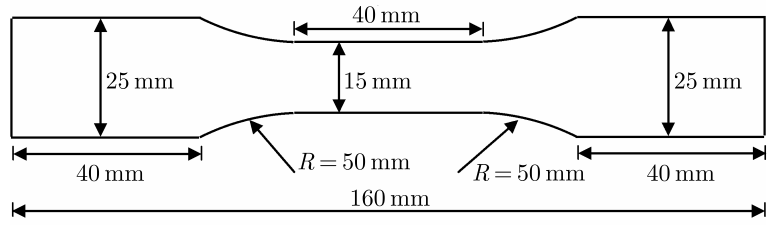

Fig. 1. Dimensions of the tensile specimens

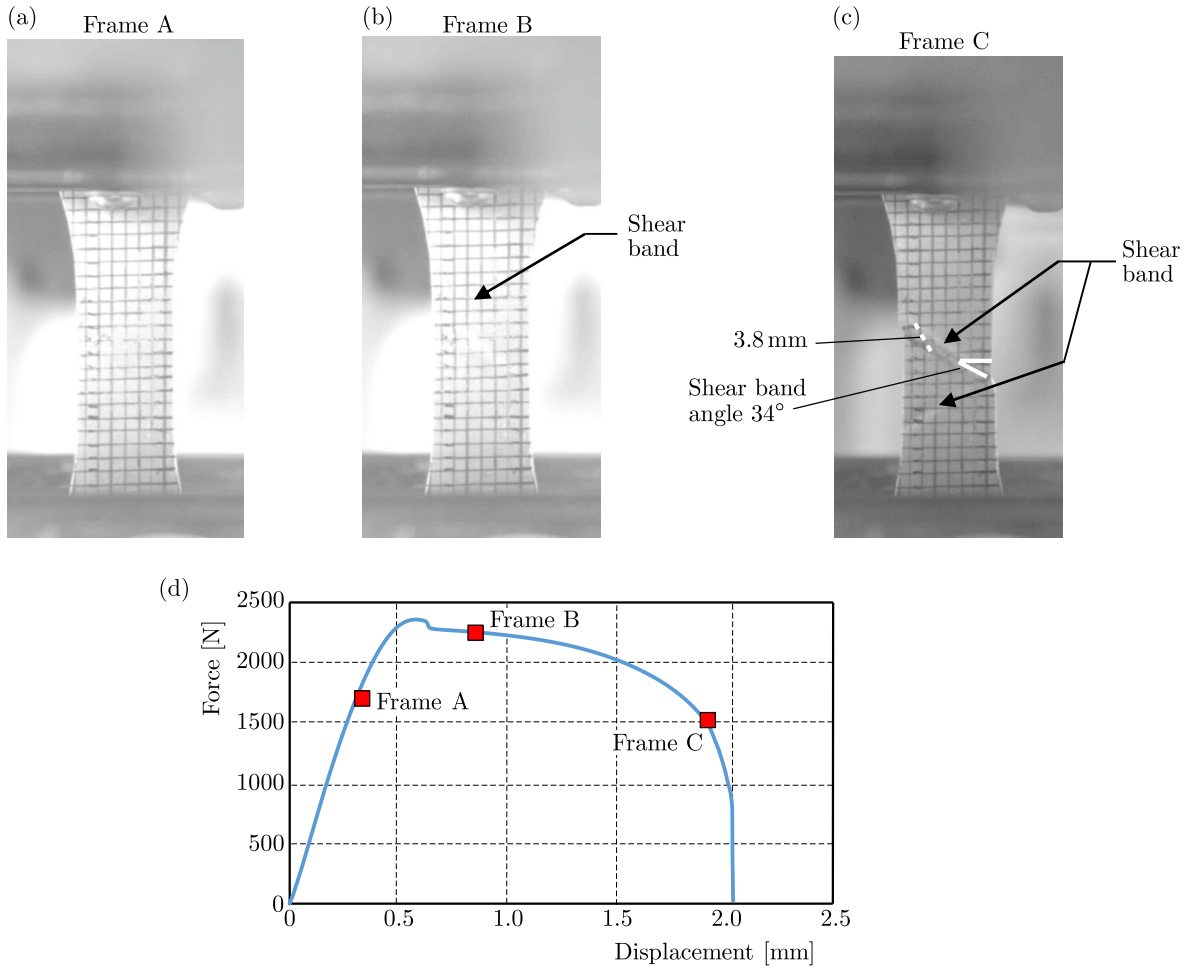

Fig. 2. Description of kinematic failure for three selected time points: (a) homogeneous deformation, elastic part, (b) strain localization $\varepsilon = 0.015$, (c) shear band before failure $\varepsilon = 0.045$, (d) force versus displacement curve for strain rate of $0.001\,\mathrm{s}^{-1}$

During the tests, an inclined fracture plane occurs along thickness of the specimens and a shear failure zone is observed along the oblique direction as Fig. 2 shows. The shear fracture is the main failure mode for AW5005 aluminum alloy subjected to quasi-static tension. A camera has been used to investigate the specimen behavior during quasi-static tensile tests. The results are given in Fig. 2 for a strain rate equal to $0.001\,\mathrm{s}^{-1}$. A set of perpendicular lines is drawn on the specimen surface with a gap of 2.25 mm between them. The tension process is recorded to estimate local deformation along the specimen loaded in tension. The failure process is presented together with the force displacement curve in Fig. 2. The analysis of the three frames A, B and C has allowed one to report the failure development of the specimen. On the frame A, the tensile process starts and the force is increasing together with the displacement. By coupling

the force and displacement measurements obtained using the hydraulic machine and the displacement observed from the camera measurement, the behavior can be defined. After the force reaches the maximum level, the process of tensile plastic strains localization starts as reported on the frame B. Finally, the plastic strain localizes, see the frame C. If the local critical failure strain is reached, a crack is formed and the measured force decreases to zero. Using local strain measurements, it is observed that the local nominal strains before the failure is close to 0.55 compared to the global strain which equals 0.1.

The quasi-static tensile tests are performed for four different strain rates, i.e. 0.001, 0.01, 0.1 and 0.15 s^{-1}. The resulting stress-strain curves are presented in Fig. 3. The experimental tests show that there is no strain rate sensitivity for aluminum alloy AW5005 behavior in the range of the strain rate used, but there is a significant difference in terms of ductility. The macroscopic true strains values at failure varies from 0.042 to 0.1. It is also observed that the ductility increases with the strain rate, Fig. 3. It shows that the average yield strength of the AW5005 aluminum is close to 147 MPa.

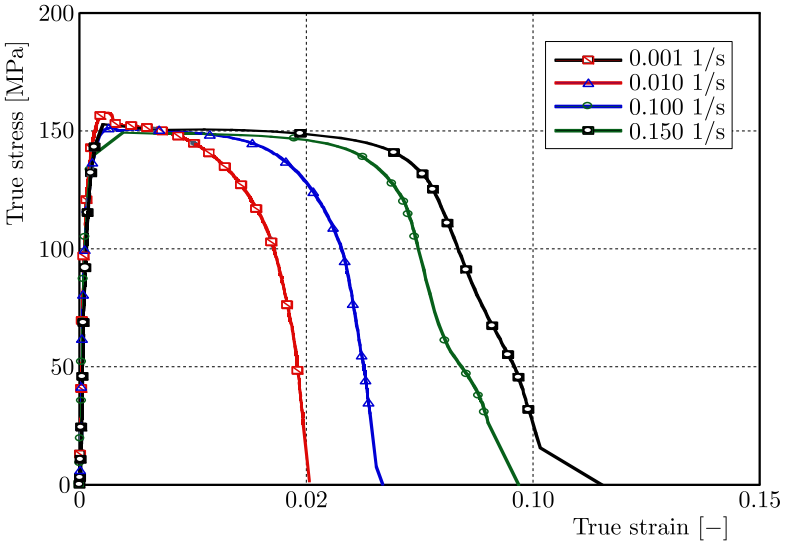

Fig. 3. Stress-strain curves for different strain rates at room temperature, aluminum AW5005

2.2. Perforation test

This part describes the mechanical behavior of aluminum sheets under impact loading. Experimental, analytical and numerical investigations have been carried out to analyze in details the perforation process (Kpenyigba *et al.*, 2013). A wide range of impact velocities from 40 to 180 m/s has been covered during the tests. A conical projectile with an angle of 72° has 13 mm in diameter and the plate is 1.0 mm thick. The active part of the specimen during perforation is presented in Fig. 4.

The projectile is launched using a pneumatic gas gun, it accelerates in the tube to reach the initial impact velocity V_0. Then, the projectile impacts the alumium sheet with partial or complete perforation depending on quantity of kinetic energy delivered to the tested plate. At the end, the residual velocity V_R of the projectile is measured after the projectile perforates the plate. Laser sensors are used to measure the initial velocity and a laser barrier for the residual velocities of the projectile during perforation. The projectile mass m_p is 28 g. The material used for machining the projectile is maraging steel with heat treatment to reach the yield stress of the projectile of 2 GPa. Therefore, the projectile is assumed as rigid during the perforation process (Kpenyigba *et al.*, 2013). The results in terms of the ballistic curve V_R-V_0 are reported in Fig. 5a.

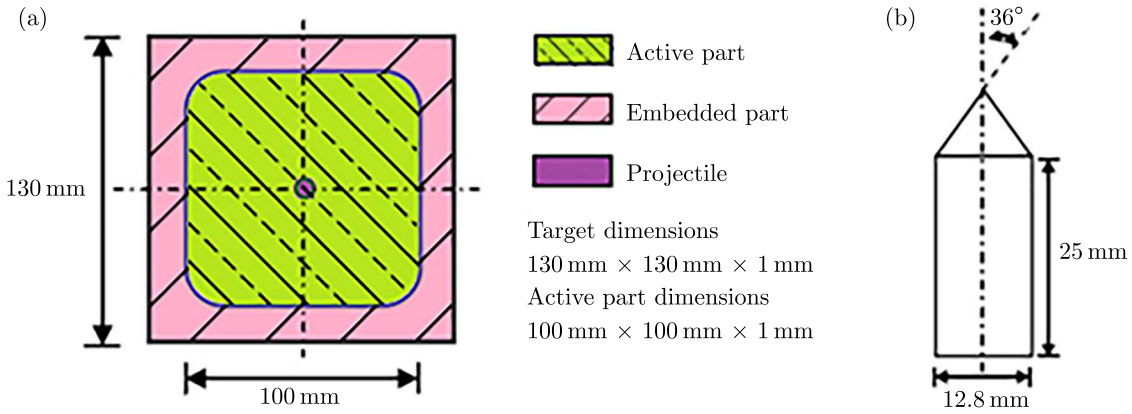

Fig. 4. Dimensions of the projectile and target used during perforation tests

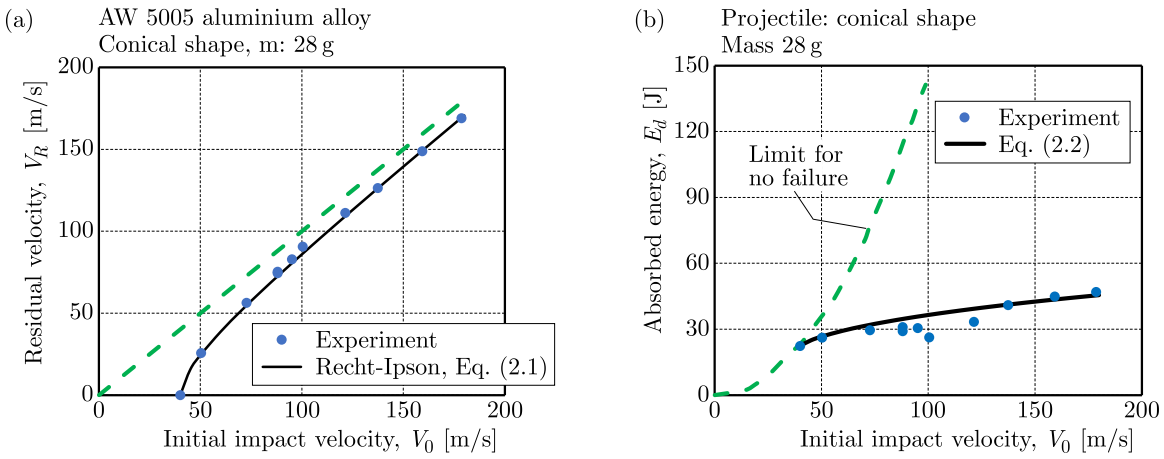

Fig. 5. (a) Ballistic curve obtained during perforation and determination of ballistic limit, (b) energy absorbed by plate during impact test, determination of failure energy

The residual velocity of the projectile can be calculated using the following equation proposed by Recht and Ipson (1963)

$$V_R = (V_0^\kappa - V_B^\kappa)^{\frac{1}{\kappa}} \tag{2.1}$$

where V_0 is the initial velocity and V_B is the ballistic velocity. In the above equation, the constants V_B is equal to 40 m/s, and κ is the ballistic curve shape parameter equal to 1.65.

The energy absorbed by the plate E_d can be calculated using the following equation

$$E_d = \frac{m_P}{2}(V_0^2 - V_R^2) \tag{2.2}$$

The difference of the initial and residual kinetic energy can be calculated using the experimental data, then based on the Recht-Ipson approximation, the energy absorbed by the plate can be calculated, see Fig. 5b. Using Eq. (2.2), the minimum energy to perforate is 28 J ($m_P = 28$ g and $V_0 = V_B = 40$ m/s).

In Fig. 6, for the initial impact velocity of $V_0 = 85$ m/s, the failure pattern is presented with four petals for the residual velocity of $V_R = 66.5$ m/s. The same failure is observed for $V_0 = 132.3$ m/s with $V_R = 120.2$ m/s, respectively. The number of petals is equal to 4 in the whole range of impact velocities, i.e. from 40 to 180 m/s. A complete description concerning the number of petals depending on the projectile shape and the failure mode was published and discussed in details in (Atkins and Liu, 1998).

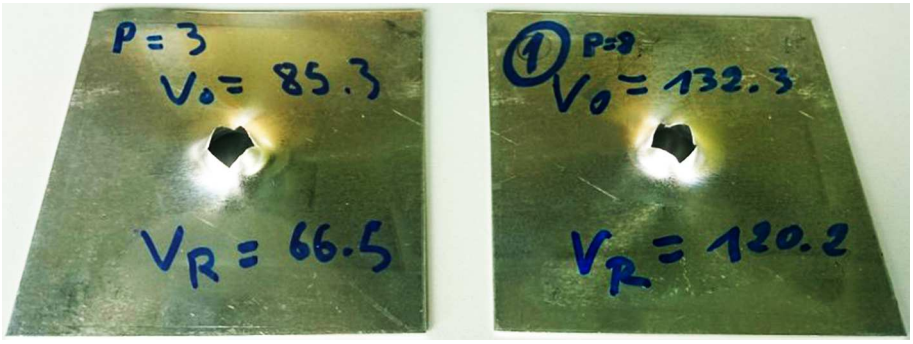

Fig. 6. Experimental observation of failure patterns, $V_0 = 85.3\,\mathrm{m/s}$ and $132.3\,\mathrm{m/s}$

3. Johnson-Cook material model

Using experimental tests, the parameters of the Johnson-Cook (JC) model (Johnson and Cook, 1983) have been identified and used to simulate tension and perforation tests. The thermo--viscoplastic behavior of AW5005 aluminum alloy is defined as follows

$$\sigma = (A + B\varepsilon_{pl}^{n})\Big(1 + C\ln\frac{\dot{\varepsilon}_{pl}}{\dot{\varepsilon}_0}\Big)(1 - T^{*m}) \tag{3.1}$$

where A is the yield stress, B and n are strain hardening coefficients, C is the strain rate sensitivity coefficient, $\dot{\varepsilon}_0$ is the strain rate reference value and m is the temperature sensitivity parameter. In this work, isothermal conditions are assumed. Therefore, the last term of the JC model related to the non-dimensional temperature T^* is not considered. All numerical simulations are done at room temperature $T = 300\,\mathrm{K}$.

The material constants are obtained by experimental tests. The parameter C has been calculated using the presented experimental tests for a quasi-static loading (strain rates from 0.001 to $0.15\,\mathrm{s}^{-1}$). In this range small strain rates sensitivity has been observed. The optimization using the minimum least square method gives the value of C equal to 0.003. These constants are shown in Table 1.

Table 1. Material parameters for the Johnson-Cook model

A [MPa]	B [MPa]	n [–]	C [–]
147	60	0.9	0.003

In order to define the material behavior completely, a failure criterion was proposed by Johnson and Cook (1985). When mixed with their classical constitutive law, Eq. (3.1), it enabled one to reflect failure modes of structures or materials.

The Johnson-Cook failure model is applied widely because of the simplicity of formulation. A number of material parameters that are available in literature were provided by Johnson and Holmquist (1989). However, Johnson and Cook only determined the positive range of the stress triaxiality based on some tensile tests and shear tests, and no small or negative values of stress triaxiality were expressed. In order to effectively apply the Johnson-Cook fracture model, researchers extended the model in different ways. Liu *et al.* (2014) proved that the Johnson-Cook fracture model can be used as damage initiation coupled with damage evolution in metal cutting simulations. Moreover, the damage evolution combines two different fracture modes effects.

In Fig. 7, the progressive damage model is used for aluminum alloy. The description includes the elastic part with E_0 (part *a*-*b*) and the plasticity range (*b*-*c*). The damage initiation with the JC criterion can be expressed by Eq. (3.2) (*c*). Along the line (*c*-*e*), the damage variable evolution grows from 0 to the maximum degradation ratio D_{max} (*d*), therefore, stiffness of the material is

degraded and reduced to $(1-D)E_0$ where D is the damage variable and E_0 is the initial Young modulus. The damage evolution is described by mesh-independent measurements (displacement at failure and damage energy dissipation) in the model. A linear evolution damage rule is used by defining a value of displacement at failure u_f (e). Thus, the maximum degradation of stiffness as well as the maximum damage have been taken finally as the failure criterion (d). The element after reaching the failure criterion is deleted from the mesh in simulation.

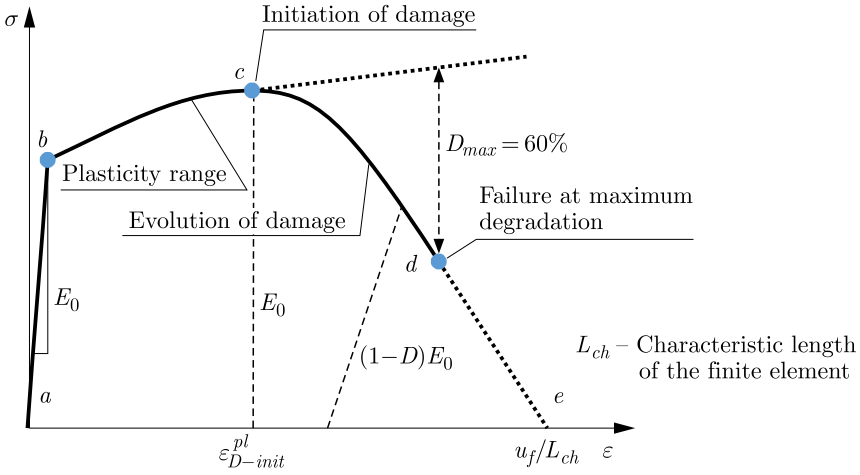

Fig. 7. Schematic representation of tensile test data in stress-displacement space for elastic-plastic materials (ABAQUS, 2011)

The Johnson-Cook damage initiation model (Johnson and Cook, 1985; Johnson and Holmquist, 1989) describes the strain at damage initiation $\varepsilon^{pl}_{D-init}$ including effects of the stress triaxiality, strain rate and temperature, as shown in the following equation

$$\varepsilon^{pl}_{D-init} = [d_1 + d_2 \exp(-d_3\eta)]\Big(1 + d_4 \ln\frac{\dot{\varepsilon}}{\dot{\varepsilon}_0}\Big)(1 + d_5 T^*) \tag{3.2}$$

where d_1, d_2, d_3, d_4, d_5 are material parameters, η is the stress triaxiality factor, $\dot{\varepsilon}_0$ is the reference strain rate and T^* is the non-dimensional temperature. The first bracket in Eq. (3.2) concerns the influence of the stress triaxiality factor on the value of strain at damage initiation $\varepsilon^{pl}_{D-init}$. The value of the first bracket decreases as the stress triaxiality factor increases. The second bracket represents the influence of the strain rate on that value, while the third one represents the effect of thermal softening.

Table 2. Failure parameters for tension and perforation

Test	Tensile test				Perforation test	
	1 ($0.001\,\mathrm{s}^{-1}$)	4 ($0.01\,\mathrm{s}^{-1}$)	3 ($0.1\,\mathrm{s}^{-1}$)	4 ($0.15\,\mathrm{s}^{-1}$)	$10^3\,\mathrm{s}^{-1}$	$10^4\,\mathrm{s}^{-1}$
Damage initiation strain $\varepsilon^{pl}_{D-init}$	0.008	0.03	0.08	0.12	0.9	0.96
Displacement at failure u_f	0.0008 m					
Max. degradation D_{max}	0.6					

By using those analytical approaches coupled to experiment results, the failure parameters have been deduced and used in the numerical model for both traction and perforation tests. They are presented in Table 2. The tensile test values are obtained from experiments, whereas the perforation test values are obtained using a numerical analysis and available literature data for similar materials (Jankowiak *et al.*, 2013, 2014; Kpenyigba *et al.*, 2013). The strain rates for perforation tests $\dot{\varepsilon} = 1000\,\mathrm{s}^{-1}$ and $\dot{\varepsilon} = 10000\,\mathrm{s}^{-1}$ correspond to initial impact velocities V_0 of 120 m/s and 180 m/s, respectively. They have been observed locally using numerical simulations.

4. Numerical approach

Numerical models are built using Abaqus/Explicit. The tests using this numerical model are conducted at different strain rates in quasi-static and dynamic conditions with impact velocities up to 180 m/s. The shell element type S4R with 8 degrees of freedom and 4 nodes with reduced integration (ABAQUS, 2011) have been used. The same element type with the element size of 0.5 mm×0.5 mm has been proposed for tension and perforation analysis as presented in Fig. 9a. The effectiveness of such elements for this type of analysis was previously proved by Ambati and Lorenzis (2016), Amiri *et al.* (2014), Elnasri and Zhao (2016).

In order to extend experimental results, some other thickness of the aluminum plate has been added for both tensile and perforation simulations, therefore, thicknesses of 1.0 mm and 1.5 mm have been used.

4.1. Modelling procedures of tensile and perforation tests

In order to verify the Johnson-Cook constitutive and failure models, tension and perforation tests have been simulated using Abaqus/Explicit version 6.14.

4.1.1. Tensile test

The aim of this numerical analysis has been to reproduce experimental results by checking the observed failure mode. The constitutive parameters have been identified based on the experimental tests. The constants are reported in Table 1. The number of elements used for meshing is 16356, and 16731 is the total number of nodes. The distribution of the equivalent plastic strains called PEEQ in Abaqus is presented in Fig. 8b.

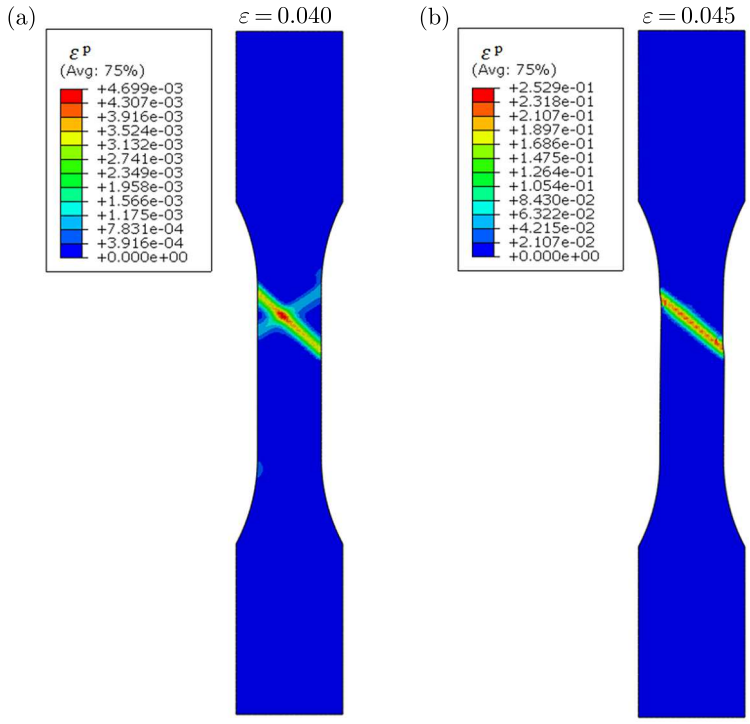

Fig. 8. Numerical simulation of tensile test, (a) equivalent plastic strain distribution for macroscopic strain equal to $\varepsilon = 0.04$, (b) equivalent plastic strain distribution for macroscopic strain $\varepsilon = 0.045$

The numerical simulations are in agreement with experimental observations where the failure mode is by shearing, see Fig. 2c.

4.1.2. Perforation test

The optimal mesh has been obtained using a convergence method (stability of the results without mesh dependency). The mesh is denser in the projectile-plate contact zone, thickness of the plate in this area is 1.0 mm and the velocity is defined in predefined fields with the range of impact velocities from 40 to 180 m/s as conceded in the experiment. This model contains 6048 elements in the central part of impact and 6161 using the same element size (0.5 mm×0.5 mm).

The ballistic curves are reported in the following Section and compared to the experimental results. The interior zone of the model allows one to initiate the process of crack propagation in a precise way. The projectile behavior has been defined as rigid, because a kinematic coupling constraint (rigid body) has been applied to avoid deformation of the projectile. The friction coefficient is assumed to be equal to 0.2.

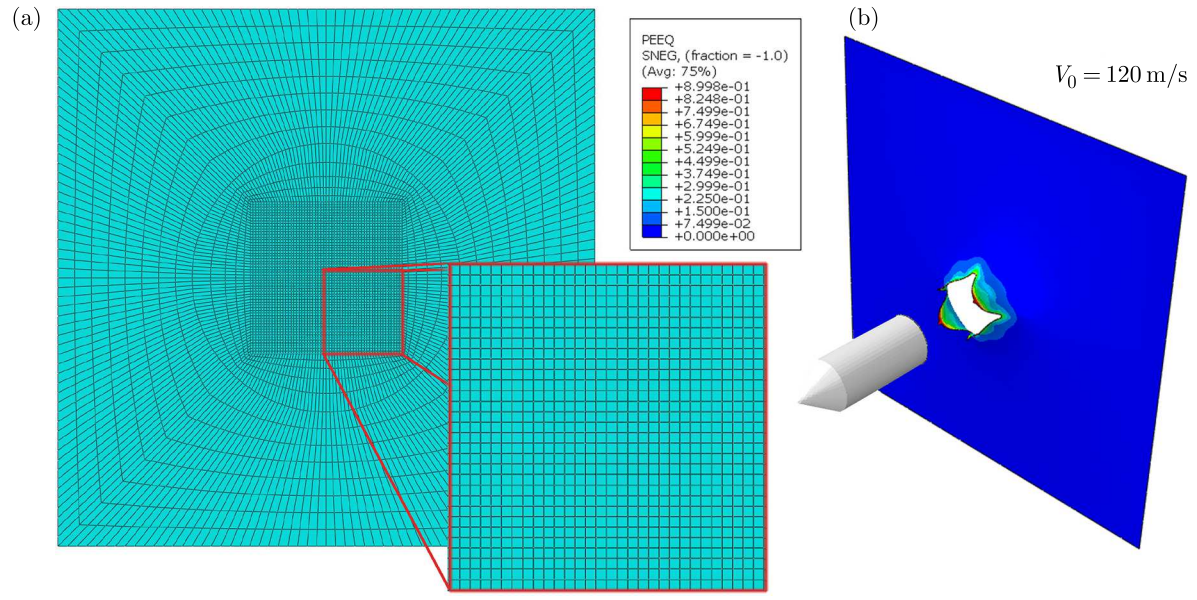

Fig. 9. Numerical model used during numerical simulations and mesh density distribution: (a) mesh, (b) equivalent plastic strain distribution for macroscopic strain ε

A decrease of the number of petals with a nose angle of 72° has been observed when the value of failure strain is changed. An analytical model for prediction of the number of petals proposed by Atkins and Liu (1998) has been used and confirmed by FE simulations.

4.2. Failure criterion model

4.3. Model I (Johnson-Cook model)

Using values illustrated in Table 2, the parameters are used to identify the Johnson-Cook damage initiation model. The triaxiality dependent part is neglected because the triaxiality in all cases is 1/3. The influence of temperature is also ignored since there is no effect on all strain rates captured by the temperature camera that have been used during the tests. The final equation used to determine the Johnson-Cook damage initiation strain $\varepsilon^{pl}_{D-init}$ as a function of strain rates $\dot{\varepsilon}$ corresponding to aluminum alloy is

$$\varepsilon^{pl}_{D-init} = [d_1]\left[1 + d_4 \ln \frac{\dot{\varepsilon}}{\dot{\varepsilon}_0}\right] \tag{4.1}$$

In order to determine the parameters d_1, d_4, an algorithm with Matlab optimization using Eq. (4.1) has been developed, and the adopted values are presented in Table 3.

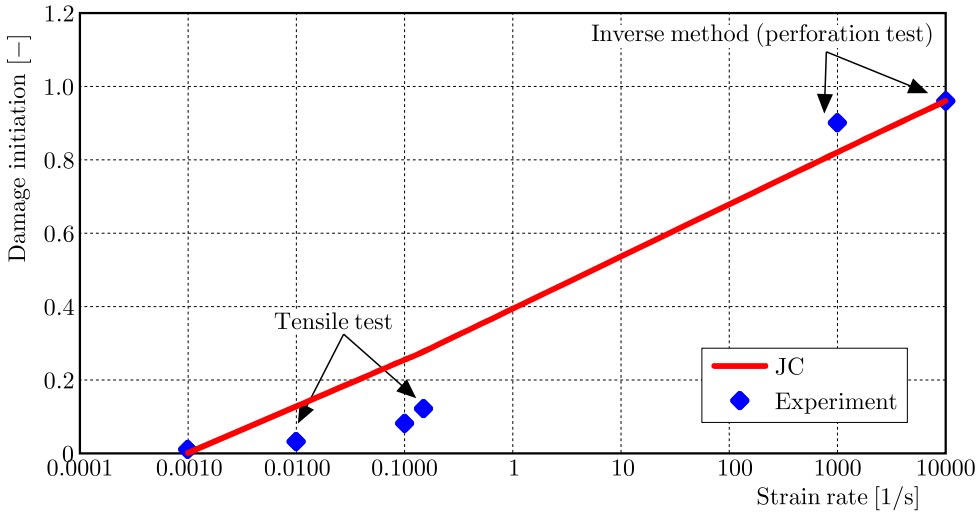

Fig. 10. Plot of damage initiation strain versus plastic strain rate using Model I JC), Eq. (4.1)

For tensile tests cases 2, 3 and 4, the damage initiation Johnson-Cook model gives too high values of the initial damage strain because it is linear in the interval of the strain rate. Finally, the global behavior in space stress-strain is too ductile, therefore, another approach has been proposed.

4.3.1. Failure modeling using optimized Model II

Another function has been proposed to better fit the damage initiation model. This function (Eq. (4.2)) contains three constants E, F and G to be determined by using an optimization algorithm. The constants are reported in Table 3

$$\varepsilon_{D-init}^{pl} = G\frac{\exp(E+F\dot{\varepsilon})}{1+\exp(E+F\dot{\varepsilon})} \tag{4.2}$$

As demonstrated in Fig. 11, there is a good correlation between the fitted curve, the experimental and numerical values, however, there is still a bit of miss-match between some points in the middle of the curve.

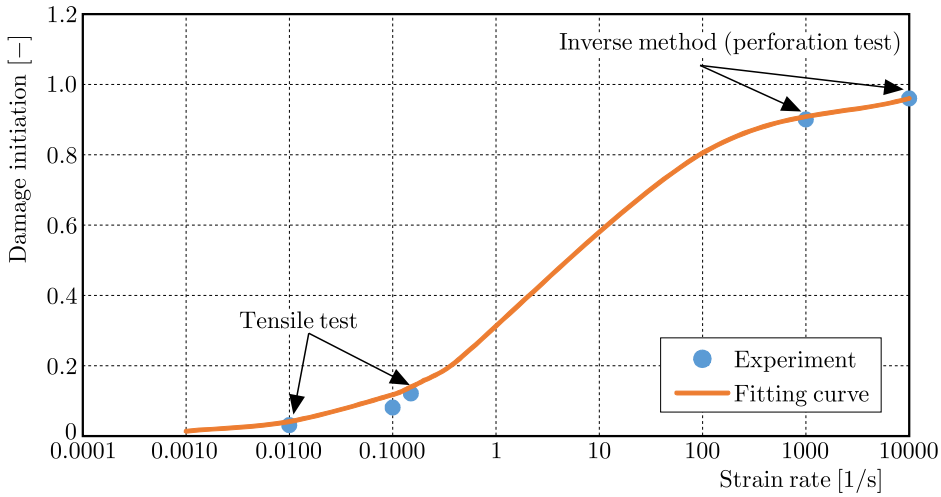

Fig. 11. Plot of damage initiation strain versus plastic strain rate using optimized Model II, Eq. (4.2)

4.3.2. Failure modeling using Model III

The next damage initiation criterion (Eq. (4.3)) is defined with two glued functions with four constants H, I, J and K. Using an optimization method, a good correlation in a wide range of strain rates is obtained (see Fig. 12)

$$\varepsilon^{pl}_{D-init} = \begin{cases} f(\dot{\varepsilon}) = H \exp(I \log_{10} \dot{\varepsilon}) & \text{if} \quad \dot{\varepsilon} \leqslant \dot{\varepsilon}_{transmition} \\ g(\dot{\varepsilon}) = J - K \exp(\log_{10} \dot{\varepsilon}) & \text{if} \quad \dot{\varepsilon} \geqslant \dot{\varepsilon}_{transmition} \end{cases} \tag{4.3}$$

The estimated constants are reported in Table 3 with $\dot{\varepsilon}_{transmition} = 1\,\mathrm{s}^{-1}$.

Table 3. Parameters for failure models

Model I (JC)		Model II			Model III			
d_1 [–]	d_4 [–]	E [–]	F [–]	G [–]	H [–]	I [–]	J [–]	K [–]
0.007	78.722	−0.89	1.13	1.0085	−0.398	1.4523	1.0085	0.6647

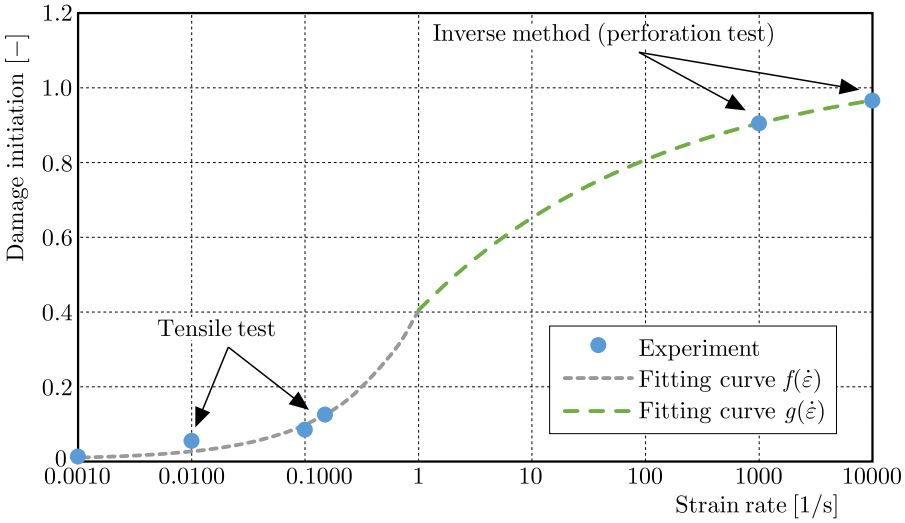

Fig. 12. Plot of failure strain versus plastic strain rate using optimized Model III

5. Comparison of numerical and experimental results

5.1. Tensile test comparisons

A comparison has been made between three initiation damage models using test number 3. As it is presented in Fig. 13, the best results are obtained with Model III. This is why this model has been adopted for an other analysis.

Initiation damage Model III has been implemented into the numerical model and then compared with the experimental data for different strain rates (0.001, 0.01, 0.1 and $0.15\,\mathrm{s}^{-1}$). The results are shown in Fig. 14.

As it might be seen in Fig. 15, there is a good correlation between the experimental and numerical results. In the case of test 3, the numerical model has demonstrated more ductile behavior at the failure start, whereas for test 4, it has revealed ductility at the terminal phase of failure.

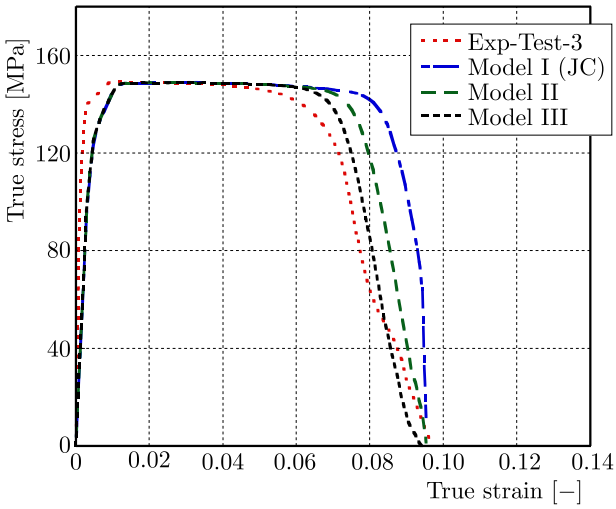

Fig. 13. Comparison between experimental and numerical curves using 3 failure criteria

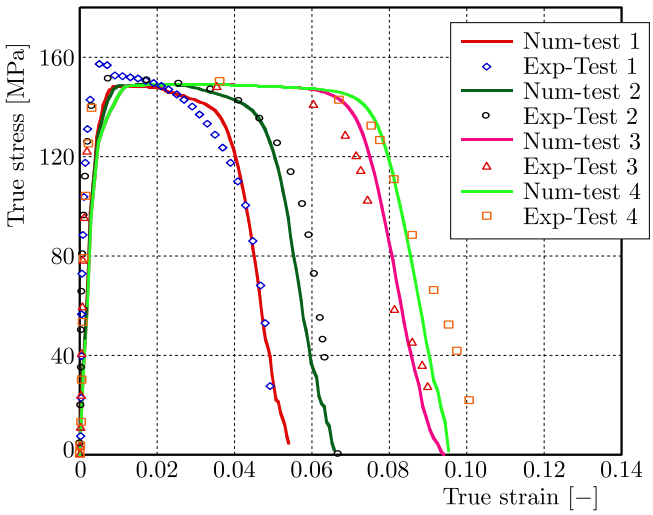

Fig. 14. Comparison between experimental and numerical curves using optimized initiation damage model (Model III)

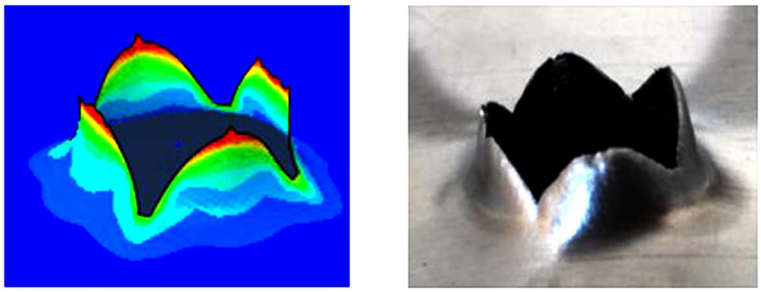

Fig. 15. Numerical result for conical projectile shape, $V_0 = 120\,\mathrm{m/s}$, comparison between experiments and simulations

5.2. Perforation test comparison

During this study, the same model (Model III) has been used to compare the numerical and experimental results in the dynamic field using the perforation process in Abaqus/Explicit with a wide range of impact velocities from 40 to 180 m/s and with target thicknesses of 1.0 and

1.5 mm. As it is shown in Fig. 15, the number of petals is the same as in the experiments, four petals are observed. It was reported in (Atkins and Liu, 1989; Landkof and Goldsmith, 1985) that the number of petals N observed during dynamic perforation coupled to a conical projectile shape was related to the nose angle ϕ. In this work, one angle (72°) has been used to analyze the results. In (Kpenyigba *et al.*, 2013) during the analysis of results it was observed that generally the number of petals N decreased when the projectile angle $\phi/2$ increased.

Figure 16 contains both the experimental and the numerical results of simulations with the same interval of velocity. Damage initiation criterion Model III has been used to verify the correlation between the numerical curve and the experiment. There is a good correlation between the experimental and numerical results which adds to the credibility of correctness of the failure criterion model. It can be observed that for thicker plates than 1.5 mm, the value of the ballistic limit is shifted from 40 m/s to 50 m/s.

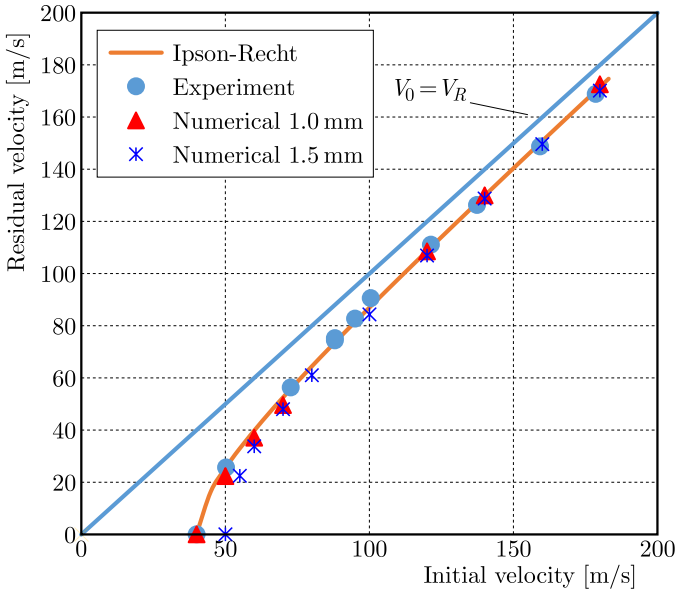

Fig. 16. The ballistic curve in experiment and in simulation

6. Conclusions

Mechanical characteristics of new aluminum alloy AW5005 have been investigated. The identification of material parameters has been done using the coupling of the simulation and experimental techniques. Additionally, three damage initiation criteria have been used in numerical modelling for both tension and perforation simulations. A good agreement has been observed between the experimental results and FE simulations in terms of the stress-strain curve and ballistic curves as well as the energy absorbed. It confirms the correctness of the damage initiation criterion.

The future work will investigate the behavior of a composite material in form of a sandwich structure with two plates of aluminum (AW5005) and one internal layer of polyethylene.

References

1. ABAQUS, Abaqus/Explicit User's Manuals, version 6.11, 2011
2. Ambati M., De Lorenzis L., 2016, Phase-field modeling of brittle and ductile fracture in shells with isogeometric NURBS-based solid-shell elements, *Computer Methods in Applied Mechanics and Engineering*, DOI: 10.1016/j.cma.2016.02.017

3. Amiri F., Millán D., Shen Y., Rabczuk T., Arroyo M., 2014, Phase-field modeling of fracture in linear thin shells, *Theoretical and Applied Fracture Mechanics*, **69**, 102-109

4. Atkins A.G., Liu J.H., 1998, Necking and radial cracking around perforations in thin sheets at normal incidence, *International Journal of Impact Engineering*, **21**, 521-539

5. Bao Y., Wierzbicki T., 2004, On fracture locus in the equivalent strain and stress triaxiality space, *International Journal of Mechanical Sciences*, **46**, 81-98

6. Børvik T., Hopperstad O.S., Langseth M., Malo K.A., 2003, Effect of target thickness in blunt projectile penetration of Weldox 460 E steel plates, *International Journal of Impact Engineering*, **28**, 413-464

7. Børvik T., Dey S., Clausen A.H., 2009, Perforation resistance of five different high-strength steel plates subjected to small-arms projectiles, *International Journal of Impact Engineering*, **36**, 948-964

8. Elnasri I., Zhao H., 2016, Impact perforation of sandwich panels with aluminum foam core: a numerical and analytical study, *International Journal of Impact Engineering*, **96**, 50-60

9. Erice B., Pérez-Martín M.J., Gálvez F., 2014, An experimental and numerical study of ductile failure under quasi-static and impact loadings of Inconel 718 nickel-base superalloy, *International Journal of Impact Engineering*, **69**, 11-24

10. Hancock J.W., Mackenzie A.C., 1976, On the mechanisms of ductile failure in high-strength steels subjected to multi-axial stress-states, *Journal of the Mechanics and Physics of Solids*, **24**, 147-160

11. Jankowiak T., Rusinek A., Kpenyigba K.M., Pesci R., 2014, Ballistic behavior of steel sheet subjected to impact and perforation, *Steel and Composite Structures*, **16**, 595-609

12. Jankowiak T., Rusinek A., Wood P., 2013, A numerical analysis of the dynamic behavior of sheet steel perforated by a conical projectile under ballistic conditions, *Finite Elements in Analysis and Design*, **65**, 39-49

13. Johnson G.R., Cook W.H., 1983, A constitutive model and data for metals subjected to large strains, high strain rates and high temperatures, *Proceedings of the 7th International Symposium on Ballistics*, **21**, 541-547

14. Johnson G.R., Cook W.H., 1985, Fracture characteristics of three metals subjected to various strains, strain rates, temperatures and pressures, *Engineering Fracture Mechanics*, **21**, 1, 31-48

15. Johnson G.R., Holmquist T.J., 1989, Test data and computational strength and fracture model constants for 23 materials subjected to large strains, high strain rates, and high temperatures. Los Alamos National Laboratory, Los Alamos, NM, Report No. LA-11463-MS

16. Kpenyigba K.M., Jankowiak T., Rusinek A., Pesci R., 2013, Influence of projectile shape on dynamic behavior of steel sheet subjected to impact and perforation, *Thin-Walled Structures*, **65**, 93-104

17. Kulekci M.K., 2014, Effect of the process parameters on tensile shear strength of friction stir spot welded aluminum alloy (EN AW5005), *Archives of Metallurgy and Materials*, **59**, 221-224

18. Landkof, B., Goldsmith, W., 1985, Petalling of thin, metallic plates during penetration by cylindro-conical projectiles, *International Journal of Solids and Structures*, **21**, 245-266

19. Liu J., Bai Y., Xu C., 2014, Evaluation of ductile fracture models in finite element simulation of metal cutting processes, *Journal of Manufacturing Science and Engineering*, **136**, 011010

20. Quinney H., Taylor G.I., 1937, The emission of the latent energy due to previous cold working when a metal is heated, *Proceedings of the Royal Society of London. Series A, Mathematical and Physical Sciences*, 157-181

21. Recht R.F., Ipson T.W., 1963, Ballistic perforation dynamics, *Journal of Applied Mechanics*, **30**, 384-390

22. Rusinek A., Klepaczko J.R., 2001, Shear testing of a sheet steel at wide range of strain rates and a constitutive relation with strain-rate and temperature dependence of the flow stress, *International Journal of Plasticity*, **17**, 87-115

23. Rusinek A., Rodríguez-Martínez J.A., 2009, Thermo-viscoplastic constitutive relation for aluminum alloys, modeling of negative strain rate sensitivity and viscous drag effects, *Materials and Design*, **30**, 4377-4390

24. Rusinek A., Rodríguez-Martínez J.A., Arias A., Klepaczko J.R., López-Puente J., 2008, Influence of conical projectile diameter on perpendicular impact of thin steel plate, *Engineering Fracture Mechanics*, **75**, 2946-2967

25. Verleysen P., Peirs J., Van Slycken J., Faes K., Duchene L., 2011, Effect of strain rate on the forming behaviour of sheet metals, *Journal of Materials Processing Technology*, **211**, 1457-1464

26. Zhong W.Z., Rusinek A., Jankowiak T., Abed F., Bernier R., Sutter G., 2015, Influence of interfacial friction and specimen configuration in Split Hopkinson Pressure Bar system, *Tribology International*, **90**, 1-14

27. Xue L., Mock W., Belytschko T., 2010, Penetration of DH-36 steel plates with and without polyurea coating, *Mechanics of Materials*, **42**, 981-1003

28. Zhong W.Z., Mbarek I.A., Rusinek A., Bernier R., Jankowiak T., Sutter G., 2016, Development of an experimental set-up for dynamic force measurements during impact and perforation, coupling to numerical simulations, *International Journal of Impact Engineering*, **91**, 102-115

Manuscript received January 3, 2017; accepted for print May 9, 2017